



Hybrid higher-order skin-topological effect in hyperbolic latticesJunsong Sun *School of Physics, Beihang University, Beijing 100191, China*

Chang-An Li*

*Institute for Theoretical Physics and Astrophysics, University of Würzburg, 97074 Würzburg, Germany*Shiping Feng *Department of Physics, Beijing Normal University, Beijing 100875, China*Huaiming Guo[†]*School of Physics, Beihang University, Beijing 100191, China*

(Received 4 June 2023; revised 26 July 2023; accepted 28 July 2023; published 9 August 2023)

We investigate the non-Hermitian Haldane model on hyperbolic $\{8, 3\}$ and $\{12, 3\}$ lattices and showcase its intriguing topological properties in the simultaneous presence of non-Hermitian effect and hyperbolic geometry. From bulk descriptions of the system, we calculate the real-space non-Hermitian Chern numbers by generalizing the method from its Hermitian counterpart and present a corresponding phase diagram of the model. For boundaries, we find that skin-topological modes appear in the range of the bulk energy gap under certain boundary conditions, which can be explained by an effective one-dimensional zigzag chain model mapped from a hyperbolic lattice boundary. Remarkably, these skin-topological modes are localized at specific corners of the boundary, constituting a hybrid higher-order skin-topological effect on hyperbolic lattices.

DOI: [10.1103/PhysRevB.108.075122](https://doi.org/10.1103/PhysRevB.108.075122)**I. INTRODUCTION**

The non-Hermitian system is a nonconservative open system [1] in which many unique physical phenomena that have no counterpart in the Hermitian case can emerge. Complex eigenvalues are allowed in non-Hermitian systems and exceptional points at which both eigenvalues and eigenstates coalesce can appear [1,2]. The coexistence of non-Hermitian effect and topology has resulted in many exotic non-Hermitian phenomena being discovered and reinterpreted [3–20]. Non-Hermitian skin effect [21–24] is a prominent example among them, that is, all eigenstates are localized to open boundaries of the non-Hermitian system. The non-Hermitian skin effect breaks down the usual bulk-boundary correspondence predicted by the Bloch theory [21,25]. A non-Bloch theory based on the generalized Brillouin zone [21,26–28] is developed to remedy the bulk-boundary correspondence in non-Hermitian systems. Interestingly, it is also found that the interplay between non-Hermitian skin effect and the topological boundary state can give rise to skin-topological modes [29], the so-called hybrid higher-order skin-topological effect [29–38].

Recently, the hyperbolic lattice has attracted considerable interest [39–55]. The hyperbolic lattice is a lattice that exists in a space of constant negative curvature. One can tessellate hyperbolic planes with any regular p -side polygon with

$p > 2$, unlike in a two-dimensional Euclidean plane where only three regular p -side ($p = 3, 4, 6$) polygon tessellation can exist. With the experimental realization of hyperbolic lattices in circuit quantum electrodynamics [39] and electric circuits [44,46], this greatly inspired the research interest in hyperbolic lattice, such as the topological properties of hyperbolic lattice [40,47], Chern insulator [48,55], high-order topological insulator [49,50], and hyperbolic band theory [41,43,51,53], etc. So far, most of the research efforts on non-Hermitian effect have focused on the lattice in Euclidean space but little attention has been paid to the corresponding effect in hyperbolic lattices. Stimulated by the experimental realization of hyperbolic lattices and rich topological physics in non-Hermitian systems, we explore the non-Hermitian topological effects on hyperbolic lattices in this paper.

We extend the non-Hermitian Haldane model to hyperbolic lattices (including hyperbolic $\{8, 3\}$ and $\{12, 3\}$ lattices), and systematically study the topological properties under non-Hermitian effects [30]. By calculating the real-space non-Hermitian Chern number, we present a phase diagram for the model in related parameter space. We also verify the topological robustness of corresponding boundary states against Anderson disorder by the localization index called the inverse participation ratio (IPR). As such, we prove the exotic topological properties in the non-Hermitian Haldane model on both hyperbolic $\{8, 3\}$ and $\{12, 3\}$ lattices from bulk as well as boundary descriptions. Remarkably, we find that the non-Hermitian effect will drive the one-dimensional topological boundary states to skin-topological modes at the

*changan.li@uni-wuerzburg.de

[†]hmguo@buaa.edu.cn

corners, forming a hybrid higher-order skin-topological effect. We explain the appearance of such a hybrid higher-order skin-topological effect by a one-dimensional zigzag chain model mapped from the specific boundary conditions of hyperbolic lattices.

The rest of this paper is organized as follows. Section II introduces the non-Hermitian Haldane model Hamiltonian. Section III investigates topological properties of the non-Hermitian Haldane model and their robustness against disorder on the hyperbolic $\{8, 3\}$ lattice. Section III presents the appearance of the hybrid higher-order skin-topological effect and its explanation. Section IV generalizes our main results to the hyperbolic $\{12, 3\}$ lattice. Finally, we provide some further discussion and conclusions in Sec. V.

II. NON-HERMITIAN HYPERBOLIC HALDANE MODEL

We consider a non-Hermitian version of the celebrated Haldane model on the hyperbolic lattice [56],

$$H = t_1 \sum_{\langle i,j \rangle} c_i^\dagger c_j + t_2 \sum_{\langle\langle i,j \rangle\rangle} e^{iv_{ij}\phi} c_i^\dagger c_j + (m + i\gamma) \sum_{i \in A} c_i^\dagger c_i - (m + i\gamma) \sum_{i \in B} c_i^\dagger c_i, \quad (1)$$

where c_i^\dagger (c_i) is the creation (annihilation) operator of electron at site i . The first term is the nearest-neighbor hopping with the amplitude t_1 . The second term represents a complex next-nearest-neighbor (NNN) hopping with an amplitude t_2 and a phase $v_{ij}\phi$. The value of v_{ij} is $+1(-1)$ for the hopping in the clockwise (counterclockwise) direction. The phase ϕ is proportional to the flux enclosed by the cyclic NNN hoppings, and we set $\phi = \pi/2$ throughout the paper. m and $i\gamma$ in the third term are real and imaginary on-site stagger potentials, respectively. The Hamiltonian is made non-Hermitian by the imaginary part of the potential, which is related to the on-site energy gain and loss. We first consider the Hamiltonian in Eq. (1) on a hyperbolic $\{8, 3\}$ lattice [see Fig. 1(a) for the geometry]. The Hermitian case, i.e., $\gamma = 0$, has been examined in a recent work [47]. It is found that while the real staggered potential only results in a trivial insulator at half filling, the NNN spin-orbit coupling opens two topological gaps located above and below $\text{Re}(E) = 0$, respectively. The resulting topological phases are characterized by nontrivial Chern numbers and chiral edge states.

Figure 1(b) plots the energy spectrum of a case of $\gamma \neq 0$ and $m = 0$ on a circular flake of hyperbolic $\{8, 3\}$ lattice. Due to the non-Hermitian nature of the Hamiltonian, the eigenvalues are complex and thus are demonstrated as points in the $[\text{Re}(E), \text{Im}(E)]$ plane. Under the basis $\Psi = (\psi_1^A, \dots, \psi_N^A, \psi_1^B, \dots, \psi_N^B)^\top$, the Hamiltonian in real space can be written as $H = \Psi^\dagger \mathcal{H} \Psi$. It can be verified that the matrix \mathcal{H} satisfies a pseudo-Hermitian condition [57],

$$\eta \mathcal{H} \eta = \mathcal{H}^\dagger, \quad (2)$$

where

$$\eta = \begin{bmatrix} 0 & I_N \\ I_N & 0 \end{bmatrix}, \quad (3)$$

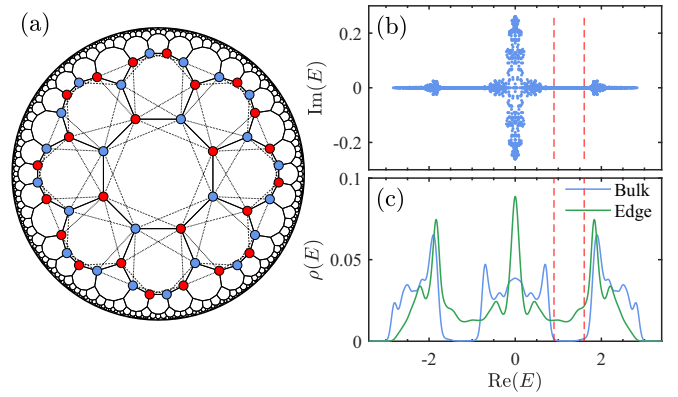


FIG. 1. (a) Schematic illustration of the Haldane model on a hyperbolic $\{8, 3\}$ lattice. The black dashed lines indicate the next-nearest-neighbor hoppings with amplitudes $t_2 e^{\pm i\phi}$. The sign of ϕ is positive (negative) for the (opposite) direction marked by the arrow, which arises due to an alternating magnetic flux. (b) Energy spectrum of the Hamiltonian in Eq. (1) on a hyperbolic $\{8, 3\}$ lattice with open boundary condition. (c) The corresponding density of states of bulk (blue) and edge (green) states. The red dotted lines in (b) and (c) estimate the topological gap above the energy $\text{Re}(E) = 0$ (the lower one is symmetric). Here the parameters in (b) and (c) are $t_1 = 1$, $t_2 = 0.2$, $m = 0$, and $\gamma = 0.3$.

and I_N is a $N \times N$ identity matrix. Suppose \mathcal{H} has a complex eigenvalue E_j with the eigenvector φ_j , which satisfies $E_j = \langle \varphi_j | \mathcal{H} | \varphi_j \rangle$. By a Hermitian operation, we get

$$E_j^* = \langle \varphi_j^* | \mathcal{H}^\dagger | \varphi_j^* \rangle = \langle \varphi_j^* | \eta \mathcal{H} \eta | \varphi_j^* \rangle. \quad (4)$$

This implies E_j^* is also an eigenvalue of \mathcal{H} with the corresponding eigenvector $\eta | \varphi_j^* \rangle$. Hence, the complex eigenvalues appear in conjugate pairs, resulting in the mirror-symmetric spectrum about the x axis.

In the next section, we calculate the corresponding density of states. Since a circular flake geometry is considered, we would like to distinguish the contributions from the bulk and edge states. For the j th eigenvector $|\varphi_j\rangle = \{\phi_{j,x}\}_{x \in N_{\text{sites}}}$, we define the bulk weight ω_j^{bulk} and the edge one ω_j^{edge} :

$$\omega_j^{\text{bulk}} = \sum_{x \in N_{\text{bulk}}} |\phi_{j,x}|^2, \quad \omega_j^{\text{edge}} = \sum_{x \in N_{\text{edge}}} |\phi_{j,x}|^2, \quad (5)$$

where N_{edge} is the number of sites enclosed outside a circle of 0.95 radius of the circular flake, and $N_{\text{bulk}} = 16$ counts the sites in the innermost unit cell. The bulk (edge) density of states can be extracted via

$$\rho_{\text{b(e)}}(E) = \frac{1}{N_{\text{sites}}} \sum_{j=1}^{N_{\text{sites}}} \omega_j^{\text{bulk(edge)}} \delta_\eta(E - E_j), \quad (6)$$

where we choose a Gaussian smearing function to approximate the delta function $\delta_\eta(\varepsilon) = \frac{1}{\eta\sqrt{2\pi}} \exp[-\frac{\varepsilon^2}{2\eta^2}]$. As shown in Fig. 1(c), the two symmetric energy gaps generated by the spin-orbit coupling remain even in the presence of a non-Hermitian term. In addition, there appear edge states traversing the gaps, implying the resulting non-Hermitian insulators are still topologically nontrivial.

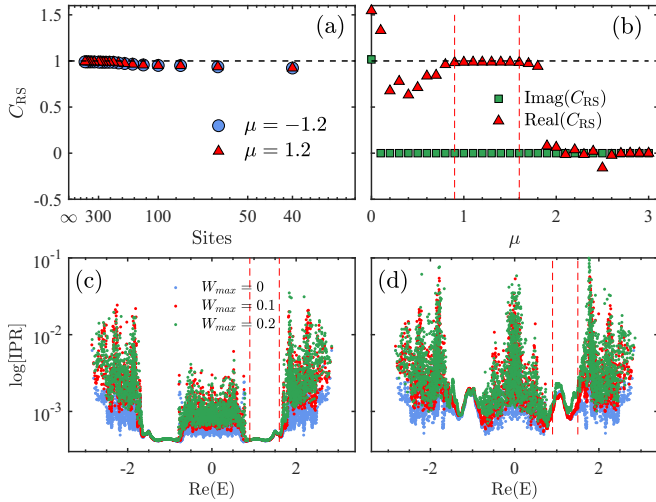


FIG. 2. (a) Convergence of the real-space Chern number for the two non-Hermitian topological phases as the lattice size increases. The blue (red) symbol represents the case that the chemical potential is located in the lower (upper) topological gap. (b) C_{RS} as a function of chemical potential μ on a hyperbolic $\{8, 3\}$ lattice with 500 sites. IPR for various disorder strengths without (c) and with (d) the non-Hermitian potential. In (c), and (a), (b), (d), the values of the imaginary potential are $\gamma = 0$ and 0.3 , respectively. The other parameters are the same as those in Fig. 1(b).

The Hermitian hyperbolic topological band insulators have been characterized by the real-space Chern number formulated as

$$C_{RS}(\mu) = 12\pi i \sum_{j \in A} \sum_{k \in B} \sum_{l \in C} \left(\mathbb{P}_{jk}^{\mu} \mathbb{P}_{kl}^{\mu} \mathbb{P}_{lj}^{\mu} - \mathbb{P}_{jl}^{\mu} \mathbb{P}_{lk}^{\mu} \mathbb{P}_{kj}^{\mu} \right), \quad (7a)$$

$$\mathbb{P}^{\mu} = \sum_{E_j < \mu} |\varphi_j^R\rangle \langle \varphi_j^L|, \quad (7b)$$

where \mathbb{P}^{μ} is the projector onto the subspace of occupied single-particle states at chemical potential μ , and A, B, C are three regions in the bulk of the systems that do not extend all the way to the boundary, and which are arranged counterclockwise around the center of the system. To apply the method to the non-Hermitian case, it is necessary to distinguish the left and right eigenvectors in constructing the projector \mathbb{P}^{μ} , which satisfy $\mathcal{H}^{\dagger}|\varphi_j^L\rangle = E_j^*|\varphi_j^L\rangle$ and $\mathcal{H}|\varphi_j^R\rangle = E_j|\varphi_j^R\rangle$, respectively [58]. Since the non-Hermitian Hamiltonian can be written as $\mathcal{H} = T \Lambda T^{-1}$ with Λ a diagonal matrix, the right and left eigenstates are just the columns of T and $(T^{-1})^{\dagger}$, and are orthonormal, i.e., $\langle \varphi_i^L | \varphi_j^R \rangle = \delta_{ij}$.

Let us first calculate the topological invariant C_{RS} when the chemical potential lies in the topological gap. As shown in Fig. 2(a), the Chern number converges to a quantized value as the size of the open hyperbolic lattice increases, indicating the non-Hermitian topological phase can be properly characterized by the definition in Eqs. (7). Then, C_{RS} as a function of chemical potential is obtained on a large enough lattice [see Fig. 2(b)]. The real-space Chern number keeps the quantized value within the topological gap, but takes zero or a random value outside the bulk gap. Hence, the appearance of the edge state is directly related to the quantization of the topological

invariant, establishing the non-Hermitian bulk-boundary correspondence. It is noted that the real-space Chern number varies continuously near the topological transition point, which should be due to the finite-size effect.

Generally, the edge states originating from the nontrivial topology are robust to the disorder that preserves the symmetry protecting the topological phase. To verify the robustness of the non-Hermitian topological edge states, we introduce a random on-site potential on each site,

$$H_{\text{dis}} = \sum_{j=1}^{N_{\text{sites}}} U_j c_j^{\dagger} c_i, \quad (8)$$

where the strength of the Anderson disorder U_j uniformly distributes in the range $[-W/2, W/2]$. The localization of an eigenstate $|\varphi_j\rangle = \{\phi_{j,x}\}_{x \in N_{\text{sites}}}$ can be characterized by the IPR [59–61], defined as

$$\text{IPR}_j = \sum_{a=1}^{N_{\text{sites}}} |\phi_{j,a}^R|^4. \quad (9)$$

The meaning of the IPR can be understood in terms of a state uniformly distributed over N sites, in which all nonvanishing elements of the wave function are $\phi_{j,a} = 1/\sqrt{N}$. According to the above definition, we have $\text{IPR}_j = 1/N$ for the homogeneous state. Hence, IPR_j can measure the number of the distributed sites of an eigenstate ($1/\text{IPR}_j$), which can be taken as a degree of its localization. In addition, since the wave function is normalized, the value is bounded by $0 < \text{IPR}_j < 1$.

To see how the IPR_j measures the localization degree of an eigenstate explicitly, we first calculate the IPR at various disorder strengths in the Hermitian case by setting $\gamma = 0$. As shown in Fig. 2(c), IPR_j s inside the two topological gaps take very small values (less than 10^{-3}), which is expected as the topological edge states are delocalized over a large number of lattice sites. In addition, IPR_j s of the edge states almost do not fluctuate and have no noticeable change with increasing the disorder strengths. In contrast, the other states have much larger IPR_j s and exhibit significant fluctuations among different eigenstates and disorder strengths, which can be viewed as the signatures of the localization.

Now we turn on the non-Hermitian potential and show the results of $\gamma = 0.3$ in Fig. 2(d). It is found that the fluctuations of IPR_j s remain very low inside the topological gaps and the values only slightly vary as the disorder strength is increased, which are in stark contrast to those in the other regions. It implies the non-Hermitian edge states are still topologically protected and they are robust against on-site disorder. However, when compared with the Hermitian counterpart, the values of IPR_j s considered here in the topological gaps are significantly increased, even in the absence of disorder. Hence, it implies possible localization of the edge states, which is related to a hybrid skin effect happening at the boundary of the hyperbolic lattice, as we will show in the next section.

Recently, the Bloch band theory has been generalized to hyperbolic lattices [41]. A hyperbolic Bravais lattice with periodic boundary conditions can be constructed by applying Fuchsian translation on the unit cell. Instead of dealing with a large real-space Hamiltonian, the single-particle spectrum can be easily obtained by diagonalizing a Hamiltonian in the momentum space (this momentum space is at least

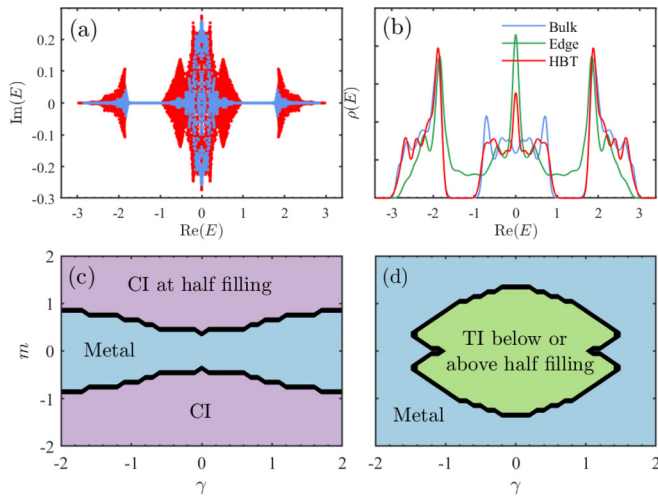


FIG. 3. (a) Energy spectrum and (b) the corresponding density of states of the Hamiltonian in Eq. (1) on a hyperbolic $\{8, 3\}$ lattice obtained by HBT (red dots or line) with periodic boundary conditions. In (a) and (b), the same quantities calculated by directly diagonalizing the Hamiltonian of an open hyperbolic flake are also plotted for comparison. The phase diagrams in the (γ, m) plane: (c) at half filling; (d) below or above half filling. CI (TI) represents conventional (topological) insulator. Here the parameters not specified are the same as those used in Fig. 1.

four-dimensional, which is unlike that of a Euclidean lattice). For the hyperbolic $\{8, 3\}$ lattice, we can choose a unit cell containing 16 sites, and thus have four independent generators to form a hyperbolic translation group (see Appendix A for details). In the four-dimensional momentum space (k_1, k_2, k_3, k_4) , the resulting hyperbolic Bloch Hamiltonian $\mathcal{H}_{\{8,3\}}(\mathbf{k})$ is a 16×16 matrix (see Appendix B for the explicit form). Since the hyperbolic band theory directly solves the bulk system, the phase diagram in the (γ, m) parameter space can be determined more precisely without the mixing of the edge states. Figure 3(a) shows the boundaries between the metal and conventional insulator (CI) at half filling. A CI can only be induced by a large enough staggered potential m , and the critical value m_c increases with the strength of the non-Hermitian potential γ .

While the topological state is absent at half filling, it appears in symmetric locations below and above the $\text{Re}(E) = 0$, as shown in Fig. 3(b). For a small γ , the topological property will be broken by a finite m . The critical value m_c decreases with increasing the absolute value of γ . As γ becomes large enough, the topological phase is completely suppressed, and the system keeps metallic at any value of m . Interestingly, near the left or right boundaries of the topological region, the topological phase can be induced by turning on m . A qualitative understanding is that the effect of the topological hopping term is manifested due to the annihilation between the real and imaginary staggered potentials.

III. HYBRID HIGHER-ORDER SKIN-TOPOLOGICAL EFFECT

In this section, we investigate the effect of the non-Hermitian potential on the edge states in the topological gap.

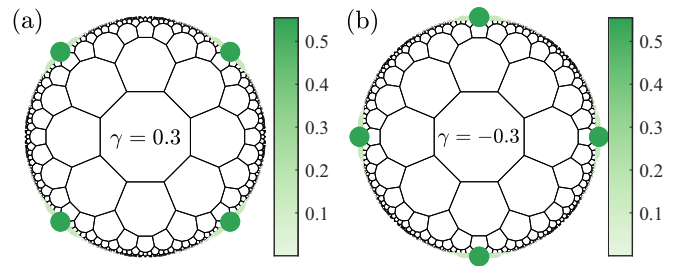


FIG. 4. Demonstration of the skin-topological corner modes in terms of the sum of the distributions of the edge states in the energy range $1 - 1.4 t_1$ for (a) $\gamma = 0.3$ and (b) $\gamma = -0.3$. The other parameters are the same as those in Fig. 1.

The on-site gain and loss drive the boundary states to localize at four corners of the disk geometry, realizing hybrid higher-order skin-topological effect. As shown in Fig. 4, the corner states are located at the diagonal positions for $\gamma > 0$ and axial positions for $\gamma < 0$. As the non-Hermitian strength γ increases, the corner modes become more localized, which should result from the strengthened non-Hermitian skin effect. This trend continues until the topological gap is closed by a large enough value of γ . The geometry considered here has an eightfold rotation symmetry and can be divided into eight equal circular sectors with central angle $\pi/4$. The corners can be regarded as the boundary sites where two adjacent pieces meet. After the staggered potential is included, the rotation symmetry is reduced to be fourfold, which accounts for the existence of localized states at four symmetric corners.

We then proceed to the underlying mechanism causing the localization of corner states. The phase ϕ in the NNN hopping results from an alternating magnetic flux piercing the hyperbolic plane perpendicularly. Similar to the celebrated Haldane model on the honeycomb lattice, the total magnetic flux in each octagon is completely canceled, and sums up to zero. However, since the boundary is composed of open-sided octagon, there exist net magnetic fluxes nearby. In the following, we will show the interplay between the nonvanishing boundary flux and the non-Hermitian physics generate a skin effect which results in the appearance of the corner modes.

For simplicity, we ignore the connections between the inner sites and the boundary ones, and model the edge state with a separate zigzag chain [see Fig. 5(c)]. The phase ϕ of the NNN hopping amplitude is positive when the electron moves in the arrow direction. If the positive directions for the two sublattices are the same and the numbers of the NNN bonds in the upper and lower chains are equal, the phases picked up by an electron circling the zigzag area through all NNN bonds are exactly canceled out, suggesting there is no net magnetic flux piercing the region. This situation occurs at a zigzag edge of the Euclidean honeycomb lattice. However, in the current paper, we have an irregular boundary which results from constructing the disk geometry using complete unit cells with the centers in a fixed radius. As shown in Fig. 5, the positive directions are not uniform anymore [to be clear, the positive direction pointing to left is denoted by red (blue) color in the upper (lower) sublattice]. The net magnetic flux is proportional to the difference in the numbers of the red arrows and the blue ones. Specifically, we focus on

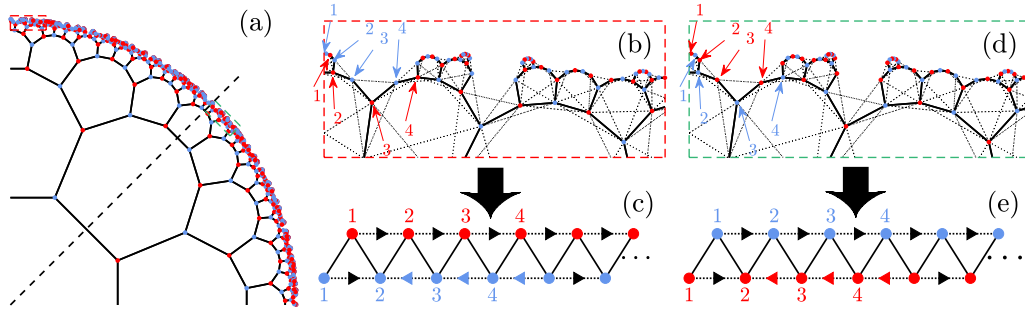


FIG. 5. (a) Illustration of the inequivalent one-fourth of the studied open hyperbolic lattice. Zoomed details of the edge geometries in the dotted line boxes located at (b) the top (red) and (d) the diagonal (green). (c) and (e) show the outermost sites arranged in zigzag shapes for the boundary fragments (b) and (d), respectively. The arrows in (c) and (e) denote the directions along which the next-nearest-neighbor hopping phase ϕ is positive.

one-fourth of the circle geometry due to the fourfold symmetry, as demonstrated in Fig. 5(a). Without the staggered potential, the upper half sector is exactly the same as the lower half one, and they are related to each other by a $\pi/4$ rotation. After γ is included, the two sectors become inequivalent and the difference is that the signs of the imaginary staggered potentials on the two sublattices are interchanged in the lower sector. The skin effect induced by a $\gamma > 0$ non-Hermitian term manifests itself in the upper sector by making all modes localize at the right end [Figs. 5(b) and 5(c)]. In contrast, due to the sign reversing of the non-Hermitian staggered potential in the lower sector, the localization from the skin effect occurs at the left end [Figs. 5(d) and 5(e)]. Hence, the two opposite localization tendencies meet at the diagonal position, generating a skin-topological corner state there. For the case of $\gamma < 0$, the localization of the skin mode changes to the opposite end of each $1/8$ sector, and the corner states appear in the axial positions.

The above skin effect can be explicitly demonstrated by examining the distributions of the eigenstates of the effective zigzag-chain Hamiltonian. We first diagonalize the non-Hermitian model mapped from the boundary of the geometry in Fig. 5(a) and find the tendency for all eigenstates to distribute near the middle ($\gamma > 0$) or ends ($\gamma < 0$) of the one-dimensional(1D) zigzag chain [Figs. 6(a) and 6(b)]. Then we proceed to consider a closed zigzag chain, which corresponds to the whole boundary of a hyperbolic disk. As shown in Fig. 6(c), there are four skin-topological corner modes and their locations are in good consistency with those obtained by the calculations on the entire lattice. The skin corner modes are induced by the imaginary staggered potential. To verify this, we plot the distributions of the eigenstates in Fig. 6(d) and indeed the corner states do not appear anymore without the non-Hermitian potential.

It is worth noting that the geometry of the boundary is critical for the appearance of the skin-topological corner modes. If the open hyperbolic flake is constructed by keeping the lattice sites located within a fixed-radius circle, the effective 1D zigzag chain is not threaded by a net magnetic flux. Consequently, the non-Hermitian potential will not lead to the skin effect, and no skin corner states are generated (see Fig. 7).

Including a comparison with the results obtained from the non-Hermitian Haldane model on the Euclidean counterpart, namely, the honeycomb lattice with Schläfli symbol

{6, 3} would be beneficial. It has been demonstrated that a hexagonal geometry with zigzag edges harbors three hybrid skin-topological modes located at the corners, which are associated with C_3 rotation symmetry [30]. Similarly, when the sign of the non-Hermitian strength changes, the location transitions to the other set of corners. While bearded edges also support corner modes, the armchair edges do not.

IV. NON-HERMITIAN HALDANE MODEL ON HYPERBOLIC {12,3} LATTICE

The hyperbolic space has an infinite number of regular tilings, each of which can be labeled by the so-called Schläfli symbol $\{p, q\}$, with p the number of sides of the polygons and q the coordination number at each vertex. Hence, we proceed further to investigate more honeycomblike hyperbolic

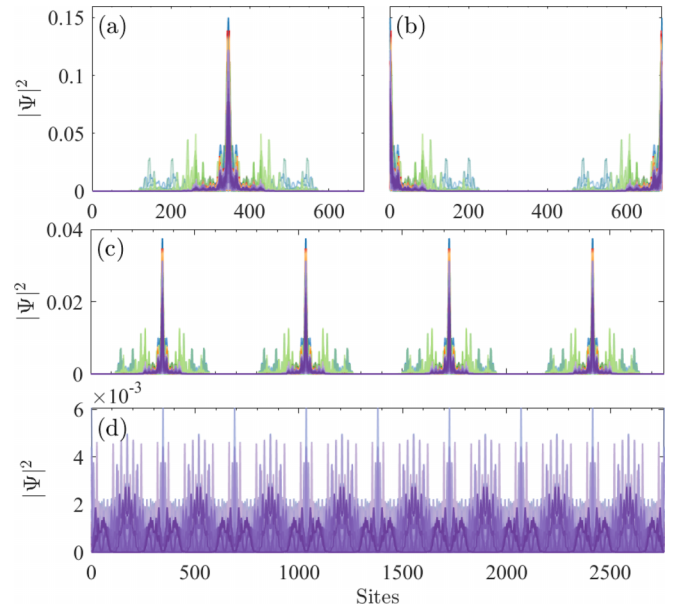


FIG. 6. The distributions of the eigenstates of the one-dimensional zigzag chain model mapped from the boundary of the inequivalent one-fourth geometry in Fig. 5(a) at (a) $\gamma = 0.8$ and (b) $\gamma = -0.8$. (c) and (d) are the distributions on a closed one-dimensional chain corresponding to the boundary of the whole hyperbolic disk with $\gamma = 0.8$ and $\gamma = 0$, respectively. The eigenstates are distinguished by different colors in (a)–(d).

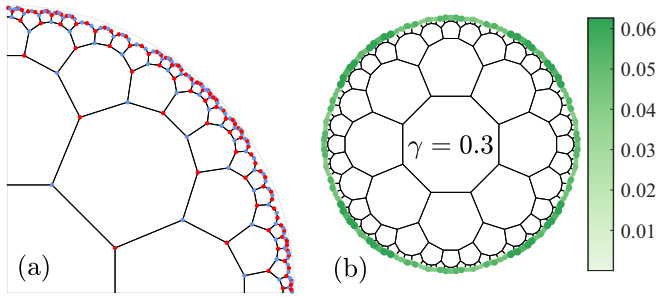


FIG. 7. (a) A smoother boundary created by cutting the hyperbolic lattice with a fixed-radius circle. (b) The distributions of the edge states in the topological energy gap at $\gamma = 0.3$, and no skin-topological corner modes are visible. The other parameters are the same as those in Fig. 1.

lattices with $p > 8$ while fixing $q = 3$ to see the evolution of the physical properties of the non-Hermitian Haldane model with a polygon geometry [see Fig. 8(a)]. The main physics, such as the topological nontrivial phase and hybrid higher-order skin-topological effect, are similar to the hyperbolic $\{8, 3\}$ presented above. For instance, the NNN spin-orbit couplings also lead to two topologically nontrivial band gaps here, which distribute symmetrically with respect to $\text{Re}(E) = 0$ [Figs. 8(b) and 8(c)]. However, a larger t_2 is needed to generate a gap with the same size in the hyperbolic $\{12, 3\}$ lattice. When the non-Hermitian term γ is introduced, the energy spectrum becomes complex and the eigenvalues come in pairs due to the pseudo-Hermiticity of the Hamiltonian. As shown in Fig. 8(c), the boundary states remain within the topological energy gap in the presence of the non-Hermitian potential, implying the topological property persists under non-Hermitian effect. We find that the real-space Chern number gets quantized in the topological gaps. In addition, these non-Hermitian edge states corresponding to nontrivial phases show robustness against on-site disorder, which suggests they are topologically protected.

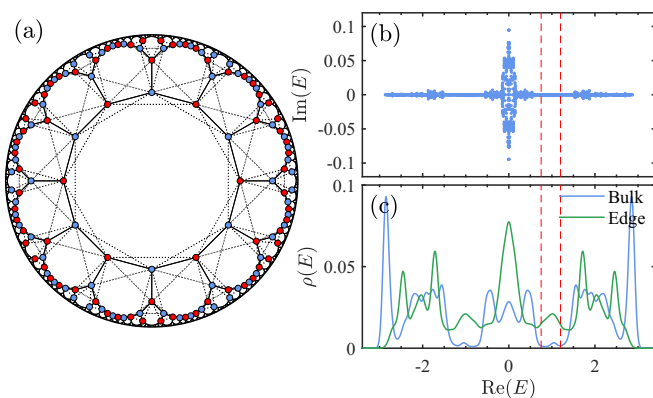


FIG. 8. (a) Schematic illustration of the Haldane model on a hyperbolic $\{12, 3\}$ lattice. (b) Energy spectrum of the non-Hermitian Haldane Hamiltonian on an open hyperbolic $\{12, 3\}$ lattice. (c) The corresponding density of states of bulk (blue) and edge (green) states. The red dotted lines in (b) and (c) estimate the topological gap above the $\text{Re}(E) = 0$ (the lower one is symmetric). Here the parameters in (b) and (c) are $t_1 = 1$, $t_2 = 0.4$, $m = 0$, and $\gamma = 0.1$.

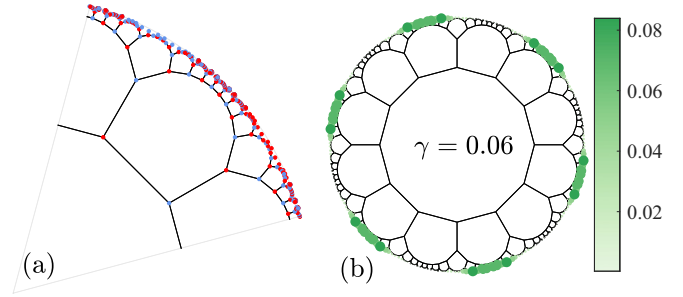


FIG. 9. (a) The inequivalent one-sixth of the open hyperbolic $\{12, 3\}$ lattice. (b) The skin-topological modes appearing symmetrically at six corners of an open hyperbolic $\{12, 3\}$ lattice.

Then we consider a disk of hyperbolic $\{12, 3\}$ lattice with an open boundary while keeping the unit cells whose centers are within a fixed radius. The positive directions of the imaginary NNN hoppings are imbalanced on the resulting boundary, near which there is a net magnetic flux threading through. Consequently, the skin-topological modes appear at six corners of the disk geometry. The six corners arise due to the sixfold rotational symmetry in the hyperbolic $\{12, 3\}$ flake. The underlying mechanism is similar as in the hyperbolic $\{8, 3\}$ case discussed previously. Let us focus on one-sixth of the geometry [see Fig. 9(a)]. Actually, this sector can be further divided into two equal parts, whose Hamiltonians are almost the same except the signs of the staggered potentials. The difference leads to the directions of the skin effects being opposite, thus generating one corner mode in each one-sixth sector [see Fig. 9(b)]. Compared to the hyperbolic $\{8, 3\}$ case, the corner modes here are more extended, which is due to the smaller net magnetic flux near the $\{12, 3\}$ boundary.

V. CONCLUSIONS AND DISCUSSION

We have investigated the topological properties of non-Hermitian Haldane model on hyperbolic lattices of two representative $\{8, 3\}$ and $\{12, 3\}$ types. We prove the existence of a nontrivial topological gap in the complex energy spectrum, characterized by a quantized non-Hermitian Chern number. Correspondingly, the edge states appear at boundaries of the hyperbolic lattices in the topological nontrivial phase. Remarkably, these edge states are driven to localize at corners of the boundary by non-Hermitian effect, forming the hybrid higher-order skin-topological effect. The mechanism accounting for such a hybrid higher-order skin-topological effect is revealed by mapping the specific boundary to an effective one-dimensional zigzag chain model with a net magnetic flux.

While we focus on hyperbolic lattices of $\{8, 3\}$ and $\{12, 3\}$ types here, the main results can be generalized to other types of different $\{p, q\}$ with similar setups. We note the number of degrees of freedom at the boundary of hyperbolic lattices is very large, different from regular lattices, such that the ratio of boundary modes over bulk modes is extremely high. Therefore, the hybrid higher-order skin-topological effect may provide an effective method to manipulate most degrees of freedom in hyperbolic lattices.

We expect the exotic non-Hermitian topology on hyperbolic lattices can be experimentally demonstrated, for

instance, in electric circuits [39,44,46,54]. Recently, the Haldane model has been successfully implemented on hyperbolic lattices using circuit networks, leading to the observation of edge states that are associated with nontrivial topology in these systems [54,62,63]. The negative resistor can introduce gain or loss into the circuit, resulting in the non-Hermitian on-site potential that is considered in this paper [64]. Therefore, the direct experimental realization of the hybrid higher-order skin-topological effect in hyperbolic lattices can be achieved through hyperbolic non-Hermitian circuits.

ACKNOWLEDGMENTS

J.S. and H.G. acknowledge support from the NSFC Grants No. 11774019 and No. 12074022. C.A.L. is financially supported by Würzburg-Dresden Cluster of Excellence ct.qmat, Project No. 390858490, and the DFG (SFB 1170). S.F. is supported by the National Key Research and Development Program of China under Grant No. 2021YFA1401803, and NSFC under Grants No. 11974051 and No. 12274036.

APPENDIX A: HYPERBOLIC GEOMETRY

In this Appendix, we present the general description of the hyperbolic geometry. The hyperbolic plane is a two-dimensional space with negative curvature. An infinitely periodic lattice on this plane can be mapped onto a unit disk $D = \{z \in \mathbb{C}, |z| < 1\}$, known as the Poincaré-disk representation [45,65]. The distance metric on the Poincaré disk is

$$ds^2 = (2\kappa)^2 \frac{dx^2 + dy^2}{(1 - |z|^2)^2}, \quad (\text{A1})$$

where κ represents the radius of curvature. From this metric, it is clear that the hyperbolic distance between two points close to each other on the edge of the unit disk in the Poincaré representation is infinite. Explicitly, it can be inferred that the hyperbolic distance between any two points, z_1 and z_2 , on the unit disk is

$$d(z_1, z_2) = \kappa \operatorname{arccosh} \left(1 + \frac{2|z_1 - z_2|^2}{(1 - |z_1|^2)(1 - |z_2|^2)} \right). \quad (\text{A2})$$

For the hyperbolic $\{p, q\}$ lattice on the hyperbolic plane, the interior angle of each regular p -gon is $2\pi/q$. If a regular p -gon is placed with its center at the origin of the Poincaré disk, then the distance from a vertex of the polygon to the center of the disk is

$$r_0 = \sqrt{\frac{\cos(\pi/p + \pi/q)}{\cos(\pi/p - \pi/q)}}. \quad (\text{A3})$$

The coordinates of these vertices can be expressed as $z_j = r_0 e^{i(2\pi j/p + \delta)}$, where $j = 1, \dots, p$, and δ an arbitrary phase factor.

For the hyperbolic $\{8, 3\}$ lattice, its unit cell consists of a regular octagon indicated by the red lines in Fig. 10(a), containing 16 sites. Therefore, the $\{8, 3\}$ lattice can be tessellated by the $\{8, 8\}$ lattice. Similarly, for the $\{12, 3\}$ lattice, one unit cell consists of a regular dodecagon containing 12 sites such that the $\{12, 3\}$ lattice can be tessellated by the $\{12, 12\}$ lattice. As long as the coordinates of the sites contained in an initial

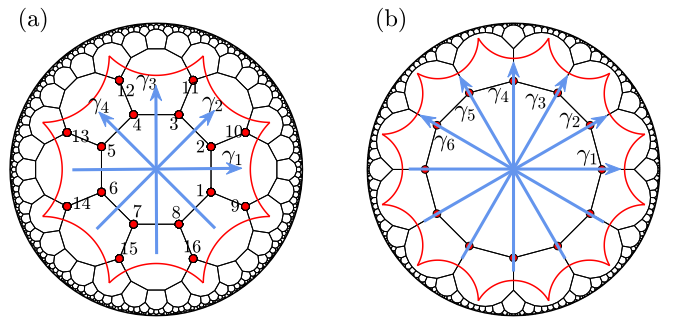


FIG. 10. Sketch of hyperbolic $\{8, 3\}$ (a) and $\{12, 3\}$ (b) lattices with marked unit cell (red dots) and fundamental domain of the Bravais lattice (red polygon), respectively. γ_j in (a) and (b) are the generators of their lattice.

unit cell are given, the coordinates of all other sites on the entire lattice can be obtained by translation operations of the sites within the unit cell. That is, any site can be uniquely represented as

$$z_i = \gamma z^{(a)}, \quad (\text{A4})$$

where a is the index of the site within the unit cell (for the $\{8, 3\}$ lattice, $a = 1, \dots, 16$), and γ is the sequence of basic translation operations that make transformations between different unit cells. The translational operator in the horizontal direction of the hyperbolic plane can be represented by the matrix

$$T(\tau) = \begin{pmatrix} \cosh(\tau/(2\kappa)) & \sinh(\tau/(2\kappa)) \\ \sinh(\tau/(2\kappa)) & \cosh(\tau/(2\kappa)) \end{pmatrix}, \quad (\text{A5})$$

with τ representing the hyperbolic distance translated horizontally by $T(\tau)$. For instance, by applying the translation operator $T(\tau)$ to the origin 0, we can utilize Eq. (A2) to calculate the distance $d(z, 0)$ between a point z and the origin, allowing us to discern the distance between the origin 0 and $T(\tau)0$ is τ . This is critical for understanding the parameter τ in the horizontal translation operation $T(\tau)$.

The unit cell on the $\{8, 3\}$ lattice contains four fundamental translation symmetry operations, also known as generators, namely, γ_m ($m = 1, 2, 3, 4$), as shown in Fig. 10. Among them, γ_1 stands for the operation that horizontally translates a unit cell to its nearest neighbor on the right.

Assuming that the hyperbolic distance from the center of the Bravais lattice to the center of a side is a , then the translation distance of γ_1 is $2a$, therefore

$$\gamma_1 = T(2a) = \begin{pmatrix} \cosh(2a/(2\kappa)) & \sinh(2a/(2\kappa)) \\ \sinh(2a/(2\kappa)) & \cosh(2a/(2\kappa)) \end{pmatrix}, \quad (\text{A6})$$

and the length of a satisfies

$$\cos\left(\frac{\pi}{p}\right) = \frac{\tanh[2\operatorname{arctanh}(a)]}{\tanh[2\operatorname{arctanh}(r_0)]}. \quad (\text{A7})$$

As long as γ_1 is known, other generators can be directly obtained through a rotation matrix:

$$R(\phi) = \begin{pmatrix} e^{i\phi/2} & 0 \\ 0 & e^{-i\phi/2} \end{pmatrix}. \quad (\text{A8})$$

Thus, we have

$$\gamma_{m=1,2,3,4} = R((m-1)\alpha)\gamma_1 R(-(m-1)\alpha), \quad (\text{A9})$$

with $\alpha = \frac{2\pi}{p_B}$ (p_B denotes the number of edges in the corresponding Bravais lattice that encompasses the unit cell).

All the translation symmetry operations of the unit cell form a Fuchsian group Γ_g . Each element in Γ_g is a sequence of operators consisting of generators and their inverses. For convenience, the inverse of a generator is also labeled as a generator, denoted by $\gamma_{p_B/2+j} = (\gamma_m)^{-1}$. Then the generator contains γ_m with $m = 1, \dots, p_B$. Each γ is a word of a specific length composed of generators, for example, a word of length n can be written as

$$\gamma = \gamma_{m_1} \cdots \gamma_{m_n}, \quad (\text{A10})$$

with $m_i = \{1, \dots, p_B\}$. What matters for γ is only the sequence of generators such that a γ can be labeled with a sequence of numbers $\vec{m} = (m_1, \dots, m_n)$. In general, any site in the lattice can be uniquely written as (a, \vec{m}) .

APPENDIX B: HYPERBOLIC BLOCH HAMILTONIAN

In this Appendix, we present the explicit form of a Bloch Hamiltonian on a hyperbolic lattice. The hyperbolic Haldane Bloch Hamiltonian $\mathcal{H}_{(8,3)}(\mathbf{k})$ is a 16×16 matrix, which can be expressed as

$$\mathcal{H}_{(8,3)}(\mathbf{k}) = H^1 + (H^1)^\dagger + H_S. \quad (\text{B1})$$

By defining $S = m + i\gamma$ and $f = e^{i\phi}$, the specific forms of matrices H_S and H^1 are given by

$$\begin{aligned} H_S &= \text{diag}(S[-1, 1, -1, 1, -1, 1, -1, 1, 1, -1, 1, -1, 1, -1, 1, -1]), \\ H_{2,1}^1 &= t_1; H_{3,2}^1 = t_1; H_{4,3}^1 = t_1; H_{5,4}^1 = t_1; H_{6,5}^1 = t_1; H_{7,6}^1 = t_1; H_{8,7}^1 = t_1; H_{1,8}^1 = t_1; \\ H_{9,1}^1 &= t_1; H_{2,10}^1 = t_1; H_{11,3}^1 = t_1; H_{4,12}^1 = t_1; H_{13,5}^1 = t_1; H_{6,14}^1 = t_1; H_{15,7}^1 = t_1; H_{8,16}^1 = t_1; \\ H_{9,14}^1 &= t_1 e^{ik_1}; H_{10,15}^1 = t_1 e^{ik_2}; H_{11,16}^1 = t_1 e^{ik_3}; H_{12,9}^1 = t_1 e^{ik_4}; \\ H_{13,10}^1 &= t_1 e^{-ik_1}; H_{14,11}^1 = t_1 e^{-ik_2}; H_{15,12}^1 = t_1 e^{-ik_3}; H_{16,13}^1 = t_1 e^{-ik_4}; \\ H_{3,1}^1 &= t_2 f; H_{4,2}^1 = t_2 f; H_{5,3}^1 = t_2 f; H_{6,4}^1 = t_2 f; H_{7,5}^1 = t_2 f; H_{8,6}^1 = t_2 f; H_{1,7}^1 = t_2 f; H_{2,8}^1 = t_2 f; \\ H_{1,10}^1 &= t_2 f; H_{2,11}^1 = t_2 f; H_{3,12}^1 = t_2 f; H_{4,13}^1 = t_2 f; H_{5,14}^1 = t_2 f; H_{6,15}^1 = t_2 f; H_{7,16}^1 = t_2 f; H_{8,9}^1 = t_2 f; \\ H_{9,2}^1 &= t_2 f; H_{10,3}^1 = t_2 f; H_{11,4}^1 = t_2 f; H_{12,5}^1 = t_2 f; H_{13,6}^1 = t_2 f; H_{14,7}^1 = t_2 f; H_{15,8}^1 = t_2 f; H_{16,1}^1 = t_2 f; \\ H_{14,1}^1 &= t_2 f e^{-ik_1}; H_{15,2}^1 = t_2 f e^{-ik_2}; H_{16,3}^1 = t_2 f e^{-ik_3}; H_{9,4}^1 = t_2 f e^{-ik_4}; \\ H_{10,5}^1 &= t_2 f e^{ik_1}; H_{11,6}^1 = t_2 f e^{ik_2}; H_{12,7}^1 = t_2 f e^{ik_3}; H_{13,8}^1 = t_2 f e^{ik_4}; \\ H_{1,12}^1 &= t_2 f e^{-ik_4}; H_{2,13}^1 = t_2 f e^{ik_1}; H_{3,14}^1 = t_2 f e^{ik_2}; H_{4,15}^1 = t_2 f e^{ik_3}; \\ H_{5,16}^1 &= t_2 f e^{ik_4}; H_{6,9}^1 = t_2 f e^{-ik_1}; H_{7,10}^1 = t_2 f e^{-ik_2}; H_{8,11}^1 = t_2 f e^{-ik_3}; \\ H_{9,11}^1 &= t_2 f e^{-ik_2+ik_1}; H_{10,12}^1 = t_2 f e^{-ik_3+ik_2}; H_{11,13}^1 = t_2 f e^{-ik_4+ik_3}; H_{12,14}^1 = t_2 f e^{ik_1+ik_4}; \\ H_{13,15}^1 &= t_2 f e^{ik_2-ik_1}; H_{14,16}^1 = t_2 f e^{ik_3-ik_2}; H_{15,9}^1 = t_2 f e^{ik_4-ik_3}; H_{16,10}^1 = t_2 f e^{-ik_1-ik_4}. \end{aligned} \quad (\text{B3})$$

For the sake of conciseness, only the nonzero matrix elements of H^1 are presented here, and the numbering scheme of the sites within the corresponding unit cell is illustrated in Fig. 10(a). The rest of the matrix elements are zero.

-
- [1] Y. Ashida, Z. Gong, and M. Ueda, *Adv. Phys.* **69**, 249 (2020).
[2] E. J. Bergholtz, J. C. Budich, and F. K. Kunst, *Rev. Mod. Phys.* **93**, 015005 (2021).
[3] V. M. Martinez Alvarez, J. E. Barrios Vargas, and L. E. F. Foa Torres, *Phys. Rev. B* **97**, 121401(R) (2018).
[4] K. Kawabata, K. Shiozaki, and M. Ueda, *Phys. Rev. B* **98**, 165148 (2018).
[5] K. Kawabata, K. Shiozaki, M. Ueda, and M. Sato, *Phys. Rev. X* **9**, 041015 (2019).
[6] D. Leykam, K. Y. Bliokh, C. Huang, Y. D. Chong, and F. Nori, *Phys. Rev. Lett.* **118**, 040401 (2017).
[7] S. Longhi, *Phys. Rev. Lett.* **122**, 237601 (2019).
[8] J. C. Budich and E. J. Bergholtz, *Phys. Rev. Lett.* **125**, 180403 (2020).
[9] C. Scheibner, W. T. M. Irvine, and V. Vitelli, *Phys. Rev. Lett.* **125**, 118001 (2020).
[10] D. S. Borgnia, A. J. Kruchkov, and R.-J. Slager, *Phys. Rev. Lett.* **124**, 056802 (2020).
[11] L. Li, C. H. Lee, and J. Gong, *Phys. Rev. Lett.* **124**, 250402 (2020).
[12] H. Xue, Q. Wang, B. Zhang, and Y. D. Chong, *Phys. Rev. Lett.* **124**, 236403 (2020).
[13] C.-X. Guo, C.-H. Liu, X.-M. Zhao, Y. Liu, and S. Chen, *Phys. Rev. Lett.* **127**, 116801 (2021).
[14] X.-Q. Sun, P. Zhu, and T. L. Hughes, *Phys. Rev. Lett.* **127**, 066401 (2021).
[15] Y. Long, H. Xue, and B. Zhang, *Phys. Rev. B* **105**, L100102 (2022).

- [16] K. Zhang, Z. Yang, and C. Fang, *Nat. Commun.* **13**, 2496 (2022).
- [17] T. Liu, Y.-R. Zhang, Q. Ai, Z. Gong, K. Kawabata, M. Ueda, and F. Nori, *Phys. Rev. Lett.* **122**, 076801 (2019).
- [18] X.-W. Luo and C. Zhang, *Phys. Rev. Lett.* **123**, 073601 (2019).
- [19] Y.-X. Xiao and C. T. Chan, *Phys. Rev. B* **105**, 075128 (2022).
- [20] F. Schindler, K. Gu, B. Lian, and K. Kawabata, *PRX Quantum* **4**, 030315 (2023).
- [21] S. Yao and Z. Wang, *Phys. Rev. Lett.* **121**, 086803 (2018).
- [22] X. Zhang, T. Zhang, M.-H. Lu, and Y.-F. Chen, *Adv. Phys.: X* **7**, 2109431 (2022).
- [23] N. Okuma and M. Sato, *Annu. Rev. Condens. Matter Phys.* **14**, 83 (2023).
- [24] Y. Yi and Z. Yang, *Phys. Rev. Lett.* **125**, 186802 (2020).
- [25] T. E. Lee, *Phys. Rev. Lett.* **116**, 133903 (2016).
- [26] Z. Yang, K. Zhang, C. Fang, and J. Hu, *Phys. Rev. Lett.* **125**, 226402 (2020).
- [27] S. Yao, F. Song, and Z. Wang, *Phys. Rev. Lett.* **121**, 136802 (2018).
- [28] K. Yokomizo and S. Murakami, *Phys. Rev. Lett.* **123**, 066404 (2019).
- [29] C. H. Lee, L. Li, and J. Gong, *Phys. Rev. Lett.* **123**, 016805 (2019).
- [30] Y. Li, C. Liang, C. Wang, C. Lu, and Y.-C. Liu, *Phys. Rev. Lett.* **128**, 223903 (2022).
- [31] K. Kawabata, M. Sato, and K. Shiozaki, *Phys. Rev. B* **102**, 205118 (2020).
- [32] R. Okugawa, R. Takahashi, and K. Yokomizo, *Phys. Rev. B* **102**, 241202(R) (2020).
- [33] Y. Fu, J. Hu, and S. Wan, *Phys. Rev. B* **103**, 045420 (2021).
- [34] X. Zhang, Y. Tian, J.-H. Jiang, M.-H. Lu, and Y.-F. Chen, *Nat. Commun.* **12**, 5377 (2021).
- [35] R. Okugawa, R. Takahashi, and K. Yokomizo, *Phys. Rev. B* **103**, 205205 (2021).
- [36] D. Zou, T. Chen, W. He, J. Bao, C. H. Lee, H. Sun, and X. Zhang, *Nat. Commun.* **12**, 7201 (2021).
- [37] W. Zhu and J. Gong, *Phys. Rev. B* **106**, 035425 (2022).
- [38] C.-A. Li, B. Trauzettel, T. Neupert, and S.-B. Zhang, *arXiv:2212.14691*.
- [39] A. J. Kollár, M. Fitzpatrick, and A. A. Houck, *Nature (London)* **571**, 45 (2019).
- [40] S. Yu, X. Piao, and N. Park, *Phys. Rev. Lett.* **125**, 053901 (2020).
- [41] J. Maciejko and S. Rayan, *Sci. Adv.* **7**, eabe9170 (2021).
- [42] X. Zhu, J. Guo, N. P. Breuckmann, H. Guo, and S. Feng, *J. Phys.: Condens. Matter* **33**, 335602 (2021).
- [43] J. Maciejko and S. Rayan, *Proc. Natl. Acad. Sci. USA* **119**, e2116869119 (2022).
- [44] W. Zhang, H. Yuan, N. Sun, H. Sun, and X. Zhang, *Nat. Commun.* **13**, 2937 (2022).
- [45] I. Boettcher, A. V. Gorshkov, A. J. Kollár, J. Maciejko, S. Rayan, and R. Thomale, *Phys. Rev. B* **105**, 125118 (2022).
- [46] P. M. Lenggenhager, A. Stegmaier, L. K. Upreti, T. Hofmann, T. Helbig, A. Vollhardt, M. Greiter, C. H. Lee, S. Imhof, H. Brand *et al.*, *Nat. Commun.* **13**, 4373 (2022).
- [47] D. M. Urwyler, P. M. Lenggenhager, I. Boettcher, R. Thomale, T. Neupert, and T. c. v. Bzdušek, *Phys. Rev. Lett.* **129**, 246402 (2022).
- [48] Z.-R. Liu, C.-B. Hua, T. Peng, and B. Zhou, *Phys. Rev. B* **105**, 245301 (2022).
- [49] Z.-R. Liu, C.-B. Hua, T. Peng, R. Chen, and B. Zhou, *Phys. Rev. B* **107**, 125302 (2023).
- [50] Y.-L. Tao and Y. Xu, *Phys. Rev. B* **107**, 184201 (2023).
- [51] N. Cheng, F. Serafin, J. McInerney, Z. Rocklin, K. Sun, and X. Mao, *Phys. Rev. Lett.* **129**, 088002 (2022).
- [52] R. Mosseri, R. Vogeler, and J. Vidal, *Phys. Rev. B* **106**, 155120 (2022).
- [53] P. M. Lenggenhager, J. Maciejko, and T. Bzdušek, *arXiv:2305.04945*.
- [54] W. Zhang, F. Di, X. Zheng, H. Sun, and X. Zhang, *Nat. Commun.* **14**, 1083 (2023).
- [55] A. Chen, Y. Guan, P. M. Lenggenhager, J. Maciejko, I. Boettcher, and T. T. Bzdušek, *arXiv:2304.03273*.
- [56] F. D. M. Haldane, *Phys. Rev. Lett.* **61**, 2015 (1988).
- [57] A. Mostafazadeh, *J. Math. Phys.* **43**, 2814 (2002).
- [58] F. Song, S. Yao, and Z. Wang, *Phys. Rev. Lett.* **123**, 246801 (2019).
- [59] X. Li, X. Li, and S. Das Sarma, *Phys. Rev. B* **96**, 085119 (2017).
- [60] S. Roy, T. Mishra, B. Tanatar, and S. Basu, *Phys. Rev. Lett.* **126**, 106803 (2021).
- [61] C.-A. Li, S.-B. Zhang, J. C. Budich, and B. Trauzettel, *Phys. Rev. B* **106**, L081410 (2022).
- [62] Q. Pei, H. Yuan, W. Zhang, and X. Zhang, *Phys. Rev. B* **107**, 165145 (2023).
- [63] H. Yuan, W. Zhang, Z. Zhou, W. Wang, N. Pan, Y. Feng, H. Sun, and X. Zhang, *Adv. Sci.* **10**, 2301128 (2023).
- [64] S. Liu, S. Ma, C. Yang, L. Zhang, W. Gao, Y. J. Xiang, T. J. Cui, and S. Zhang, *Phys. Rev. Appl.* **13**, 014047 (2020).
- [65] N. Balazs and A. Voros, *Phys. Rep.* **143**, 109 (1986).